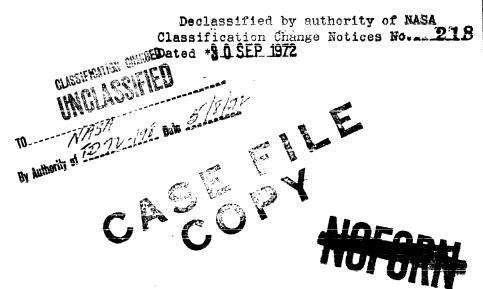


NASA TECHNICAL Memorandum



UB NASA TM X-1258

NASA TM X-1258



EXPERIMENTAL INVESTIGATION OF FLOW CHARACTERISTICS OF THE APOLLO REENTRY CONFIGURATION AT A MACH NUMBER OF 20 IN NITROGEN

by Charles G. Miller III and Pierce L. Lawing

Langley Research Center

Langley Station, Hampton, Va.

NATIONAL AERONAUTICS AND SPACE ADMINISTRATION . WASHINGTON, D. C. . JULY 1966





EXPERIMENTAL INVESTIGATION OF

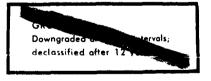
FLOW CHARACTERISTICS OF THE APOLLO REENTRY CONFIGURATION

AT A MACH NUMBER OF 20 IN NITROGEN

By Charles G. Miller III and Pierce L. Lawing



Langley Research Center
Langley Station, Hampton, Va.



CLASSIFIED DOCUMENT-TITLE UNCLASSIFIED This material contains information and the national defense of the United States within the meaning of the assertion of the states of the United States within the meaning of the assertion of the states of the states

NOTICE

The ment should not be returned after it has satisfied to the satisfied of in accordance to the appropriate provisions.

Security Manual for Safe-Guarding Classian Information.

NATIONAL AERONAUTICS AND SPACE ADMINISTRATION



EXPERIMENTAL INVESTIGATION OF

FLOW CHARACTERISTICS OF THE APOLLO REENTRY CONFIGURATION AT A MACH NUMBER OF 20 IN NITROGEN*

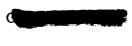
By Charles G. Miller III and Pierce L. Lawing Langley Research Center

SUMMARY

Measured pressure distributions on the forebody and afterbody of the Apollo reentry configuration along with schlieren photographs of the bow-shock-wave shapes and photographs of the afterbody tuft-flow patterns were obtained in the Langley hotshot tunnel. The investigation was performed for angles of attack of $0^{\rm O}$ and $33^{\rm O}$ at a free-stream Mach number of approximately 20 and a free-stream Reynolds number, based on maximum model diameter, of approximately $1 \times 10^{\rm 5}$ in nitrogen.

Afterbody pressure distributions and tuft studies for an angle of attack of 00 revealed that the flow remained attached around the model corner onto the afterbody and separated at a point where the ratio of the surface distance from the model axis of symmetry to the maximum model radius (s/R) was approximately 1.4. Comparison of this result with those obtained at Mach numbers 8 and 13.8 in air showed a trend of rearward movement of the point of flow separation from $s/R \approx 1.1$ at Mach 8 to $s/R \approx 1.4$ at Mach 20. The afterbody surface pressure in the attached flow region for a 00 angle of attack was approximately three times the computed free-stream static pressure and approximately 30 percent greater than the prediction of Prandtl-Meyer theory for attached flow. The afterbody surface pressure in the separation region was constant with the ratio s/R and was approximately 10 times the free-stream pressure. The tuft results indicated reverse flow in the separation region. For a 330 angle of attack, comparison of the afterbody pressure distribution along the most windward meridian with flat-plate results obtained at a Mach number of 20 showed that the afterbody pressure distribution would probably compare favorably with that of a blunt-leading-edge flat plate having a leading-edge radius equal to the Apollo corner radius. Blast-wave theory adequately predicted the afterbody pressure distribution along the most windward meridian. Differences in the point of flow separation and the angle of flow separation between the present results for 00 angle of attack and those obtained at Mach 20 in helium showed that helium simulation of Apollo afterbody flow expansion characteristics in air or nitrogen is not feasible for this Mach number regime.

^{*}Title, Unclassified.



INTRODUCTION

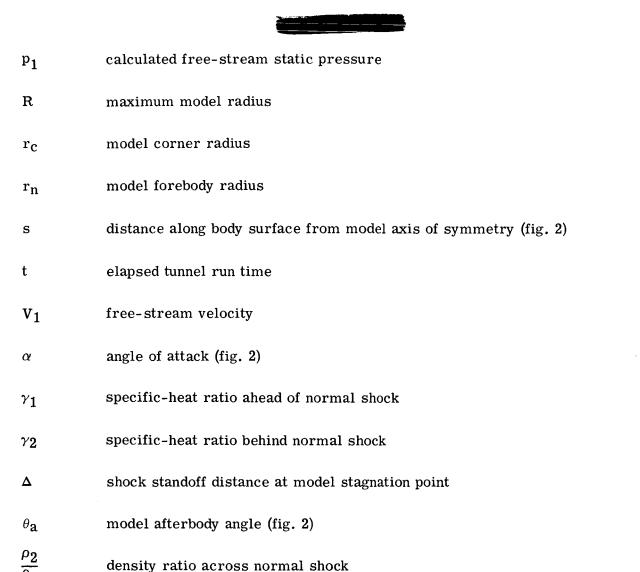
One of the current reentry vehicles of interest, from both practical and academic standpoints, is the Apollo spacecraft. Although numerous aerodynamic investigations have been conducted on the Apollo configuration for Mach numbers less than 14 in air (refs. 1 to 8) and Mach numbers from 10 to 24.5 in helium (refs. 6, 9, 10, and 11), very little pressure data, particularly on the afterbody, have been obtained for the Mach 20 regime in air or nitrogen (ref. 12). The scarcity of Apollo data in the earth-entry regime simulated by the Langley hotshot tunnel and the possible existence of discrepancies between air or nitrogen and helium results due to differences in specific-heat ratios in this regime led to the present investigation. The investigation, performed for $0^{\rm O}$ and $33^{\rm O}$ angles of attack, includes measured forebody and afterbody pressure distributions, schlieren photographs of the bow-shock-wave shapes, and photographs of the afterbody tuft-flow patterns on the Apollo configuration at a free-stream Mach number of approximately 20 and a free-stream Reynolds number, based on maximum model diameter, of approximately 1×10^5 . A comparison of existing pressure data obtained at Mach numbers from 6 to 20 in air and nitrogen and from 10 to 24.5 in helium for supportmounted and free-flight test models is also included in the investigation.

SYMBOLS

The units used for the physical quantities defined in this paper are given both in the U.S. Customary Units and in the International System of Units (SI). Factors relating the two systems are given in the appendix.

| a | point of tangency of model corner with free-stream flow direction for |
|---|---|
| | $\alpha = 0^{\circ}$ (s/R = 1.077) |

- D maximum model diameter
- M₁ free-stream Mach number
- N_{Re,D} free-stream Reynolds number based on maximum model diameter
- p local measured pressure
- p_s afterbody surface pressure in separation region
- $p_{t,2}$ pressure at model stagnation point for $\alpha = 0^{O}$



FACILITY AND APPARATUS

φ

angular displacement with respect to vertical plane of symmetry (fig. 2)

Facility and Tests

The Langley hotshot tunnel is a hypervelocity, arc-heated, blowdown facility. As shown in figure 1, the major components of this facility include capacitor banks, an arc chamber, a 10^o total-divergence-angle conical nozzle and test section, a 10^o conecylinder diffuser, and a vacuum reservoir. A more detailed description is presented in references 13 and 14.

A test-section free-stream Mach number of approximately 20 and a free-stream Reynolds number, based on maximum model diameter, of approximately 1×10^5 was





obtained for a nominal arc-chamber pressure of 600 atmospheres (61 MN/m^2) and stagnation temperature of 3400° R $(1900^{\circ}$ K) with nitrogen as the test gas. Tunnel calibration results are presented in reference 14.

Model and Support System

The pressure model and support are shown schematically in figure 2. The 4-inch-diameter (10.16-cm) model consisted of a detachable-spherical-segment heat shield (denoted in the present investigation as the forebody) in conjunction with a reversed blunt-cone afterbody with a 33° semiapex angle. The model was fabricated of fiber glass with a nominal wall thickness of 0.100 inch (2.54 mm). A side-mounted sharp-leading-edge strut, inclined at an angle of 37° to the nozzle axis of revolution, supported the model.

As shown in figure 3, eight pressure orifices having diameters of 0.040 inch (1.016 mm) were located on the model forebody; six of them were in the vertical plane of symmetry. The locations of the 17 afterbody pressure orifices (diameters of 0.125 inch (3.175 mm)) are also shown in the afterbody development in figure 3. Four of the orifices were located along the meridian at which $\phi = 0^{\circ}$.

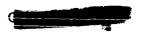
The model employed in the tuft study was geometrically identical (4-inch diameter (10.16 mm)) to the pressure model. It was a heat-transfer model being tested primarily for instrumentation evaluation and was supported by a solid steel 0.5-inch-diameter (1.27 cm) cylindrical sting inclined at an angle of 37^{O} to the nozzle axis of revolution. The tufts were positioned along the meridian at which $\phi = 0^{O}$ and their locations are shown in the afterbody development in figure 3.

Instrumentation

The short running time of the tunnel (approximately 0.1 second) and range of models surface pressures to be measured (approximately 0.002 to 1.0 psia (14 to 6895 N/m^2)) required fast-response, high-sensitivity pressure instrumentation with minimum orifice tube length. These conditions required miniaturized pressure transducers that could be mounted within the model.

The forebody surface and pitot probe pressure measurements were made with double-coil, single-diaphragm, variable-reluctance, wafer-style differential pressure transducers. (See refs. 15 and 16 for description and theory of operation.) These measurements were believed to be accurate to within ± 5.0 percent (refs. 13 and 14). The contamination trap configuration illustrated in figure 3 of reference 14 was employed to protect the forebody pressure instrumentation from flow contamination.





Afterbody surface static-pressure measurements were made with double-coil, single-diaphragm, variable-reluctance differential pressure transducers having a greater sensitivity and size than the wafer transducers. Geometric details of these pressure transducers are presented in reference 17. Because of the low magnitude of pressure anticipated on the model afterbody, the transducer pressure ports were flush mounted to minimize lag in the measurements. As shown in figure 7 of reference 17, for which the same level of pressure was experienced, there was no significant lag associated with the pressure instrumentation. The afterbody pressure transducers were mounted on rubber and held in place by rubber grommets in order to reduce mechanical vibration effects.

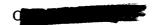
The afterbody pressure transducers were calibrated while installed in the model; the transducers were referenced to an external vacuum source by employing the model and support interior as a vacuum manifold. Calibration procedure, including a typical calibration curve, is discussed in reference 17. The afterbody pressure measurements were believed to have an accuracy of approximately ±25 percent for the magnitude of pressures measured. The variable reluctance transducers were excited by 5-volt, 20-kilocycle carrier amplifiers. The output signals from these amplifiers drove galvanometers in a light-beam type of oscillograph.

For the tuft study, strands of cotton string were positioned along the meridian at which $\phi=0^{\circ}$ on the afterbody surface (fig. 3). In an attempt to conduct an oil-flow visualization study of a very preliminary nature, a mixture of lampblack and vacuum-pump oil (2-ethylhexylsebacate) was applied to the fiber-glass model. Movements of the tufts and the lampblack-oil mixture over the model surface during a tunnel run were photographed on 16-mm film at 4200 frames per second.

DATA REDUCTION

The real-nitrogen data-reduction program presented in reference 18 was employed in the present investigation. The basic input data for this program are the initial arc-chamber density, the arc-chamber pressure, and the test-section stagnation pressure behind a normal shock. For the present tests at an angle of attack of 0° , the stagnation pressure on the model was approximately 20 percent higher than the simultaneously measured test-section pitot pressures, which were obtained with probes positioned within the calibrated inviscid test core as defined in reference 14. A probable explanation for the discrepancy between the model stagnation pressure and pitot pressures is that the nozzle boundary-layer characteristics were influenced by the relatively large-diameter blunt test configuration in that the model caused a thickening of the boundary layer such that the pitot probes no longer were within the test core. Hence, the model





stagnation pressure was employed as the test-section stagnation-pressure input for 0° angle of attack, and the pitot pressure, adjusted to an equivalent model stagnation pressure based on the 20-percent discrepancy observed for 0° angle of attack, served as the input pressure for 33° angle of attack. The validity of simplifying assumptions of this program and uncertainties associated with the computed free-stream flow parameters for the present test conditions are discussed in the appendix of reference 14. As in reference 14, vibrational equilibrium nozzle flow was assumed in this investigation. Although the pressure ratios for the present investigation were essentially constant with elapsed tunnel run time (ref. 13), the ratios were obtained every 10 milliseconds and time-averaged over the tunnel run.

RESULTS AND DISCUSSION

Shock Shapes

Representative schlieren photographs of the bow-shock-wave shapes for angles of attack of 00 and 330 are presented in figure 4. At an angle of attack of 00, the shock standoff distance at the model stagnation point predicted from reference 19 for the present density ratio $ho_2/
ho_1$ of 6.8 was 5 percent less than the present measured shock standoff distance (average of standoff distances from three schlieren photographs). The results of reference 20, which are applicable for a wider variation in body geometry and angle-of-attack range than those of reference 19 (results of ref. 19 are applicable only for angles of attack less than 250 for the Apollo configuration) predicted a shock standoff distance 10 percent less than the present measured value. For an angle of attack of 330 the findings of references 2, 9, and 20 show the stagnation point to be located where the value of s/R is approximately 0.85. As discussed in reference 9, the movement of the stagnation point would be small for the range of density ratios (4 to 6.8) and specific-heat ratios γ_2 (1.3 to 1.67) experienced in references 2 and 9 and in the present investigation. If the stagnation-point location is assumed to be at s/R = 0.85 for the present 330 angle-of-attack results, reference 20 predicted a shock standoff distance at the stagnation point 12 percent less than the present measured value.

Comparison of bow-shock shapes obtained in the present investigation with shock shapes obtained on the Apollo configuration (scaled to the present model) at a Mach number of 20 in helium (ref. 9) is made in figure 5. As expected from reference 21, the ratio of shock standoff distance to maximum model diameter at 0° angle of attack is greater for the helium results. (The density ratio for helium at a Mach number of 20 is 0.584 times the present density ratio.) The measured ratio of shock standoff distance to maximum model diameter for helium was approximately 1.48 times the measured ratio for nitrogen. This finding is within 1 percent of the prediction of reference 21 and





hence is within the reading accuracy of the present schlieren photographs and the figures of reference 9. Figure 5 shows that at angles of attack of 0° and 33° , the bowshock curvatures are similar over the forebody; however, at an angle of attack of 33° (fig. 5(b)), the shock curvatures diverge as the flow expands about the windward corner, with the nitrogen shock wave tending to lie closer to the body.

Forebody Pressure Distribution

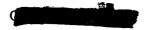
The forebody pressure distributions in the vertical plane of symmetry along with results from other investigations (refs. 1, 2, 9, 11, and 12) are presented in figure 6. Also shown are predictions obtained from modified Newtonian theory and from the theory of reference 19. The present forebody surface pressures of figure 6(a) are normalized by the model stagnation pressure and represent the average of results from three tunnel tests. These data are in reasonably good agreement with the experimental results of references 1, 2, 9, 11, and 12. The theory of reference 19 for $\gamma_2 = 1.3$ gives a good prediction of the pressure distribution and follows the pressure decrease near the forebody corner, which Newtonian theory does not do. This result is expected since Newtonian theory cannot anticipate and account for expansion around a corner.

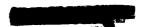
At an angle of attack of 33° (fig. 6(b)), the forebody surface pressures are normalized by the pitot pressure which is adjusted to an equivalent model stagnation pressure. With this correction, forebody pressure data for an angle of attack of 33° (fig. 6(b)) are in fair agreement with Newtonian theory and the findings of references 2, 9, 11, and 12; however, it should be noted that a smaller correction to the normalizing pressure, corresponding to a decrease in model influence on the boundary-layer characteristics, would tend to improve the agreement.

Afterbody Pressure Distribution

Afterbody surface-pressure ratios for the meridian at which $\phi = 0^{O}$ are presented in figure 7. The data for 0^{O} angle of attack (fig. 7(a)), represent the average of data from two tunnel tests.

For 0° angle of attack (fig. 7(a)), the afterbody surface pressure at s/R=1.34 is approximately three times the computed free-stream static pressure (indicated in fig. 7(a) by $p_1/p_{t,2}$). The afterbody surface pressure increases to approximately 10 times the free-stream static pressure between values of s/R of 1.34 and 1.69 and then remains constant over the rearward portion of the afterbody. The threefold increase in pressure between values of s/R of 1.34 and 1.69 is attributed to the separation of the laminar flow, which remained attached around the model corner onto the afterbody. The dashed line between the two foremost pressure measurements represents the estimated pressure trend based on tuft results to be discussed in a subsequent section.





With the assumptions of isentropic expansion around the model corner and attached flow parallel to the afterbody surface, two-dimensional Prandtl-Meyer theory (with correction for caloric imperfections) was employed to calculate the afterbody surface pressure in the attached flow region for an angle of attack of 0° . The flow-expansion angle was defined by the slope of the model surface at the sonic point (relative to the free-stream direction) and the slope of the model afterbody. If it is assumed, as in reference 2, that the slope of the model surface at the sonic point is 45° , the calculated surface-pressure ratio as shown in figure 7(a) is approximately 30 percent less than the measured ratio at s/R = 1.34. By employing the measured pressure at s/R = 1.34 and assuming an isentropic expansion and attached flow parallel to the afterbody surface, the sonic point was determined to be at s/R = 1.011, which corresponds to a model surface slope at the sonic point relative to the free-stream direction of 39° . A flow separation angle of 22° with the free-stream flow direction was computed from the measured afterbody surface pressures in the separation region.

The present results for $33^{\rm O}$ angle of attack are shown in figure 7(b). The local pressure is normalized by the pitot pressure which is corrected to an equivalent model stagnation pressure. Also shown in figure 7(b) are two-dimensional blast-wave theory and unpublished data obtained by William D. Harvey on flat-plate models having leading-edge radii of 0.001 inch (0.00254 cm) and 0.4 inch (1.016 cm) in the Langley hotshot tunnel at the same free-stream test conditions as those of the present investigation. In the blast-wave theory, the Apollo model corner radius ($\mathbf{r_c} = 0.2$ inch (0.51 cm)) was used as the thickness parameter and a value of 1.4 was used for the specific-heat ratio ahead of the normal shock γ_1 . The blast-wave theory adequately predicts the afterbody pressure distribution along the most windward meridian for the present range of s/R examined, as was observed in references 4 and 5. The Apollo afterbody surface pressure distribution for $33^{\rm O}$ angle of attack and $\phi = 0^{\rm O}$ is similar to that of the blunt-leading-edge flat plate, an indication of attached flow along the most windward meridian. Thus the Apollo afterbody surface pressure distribution would be expected to compare favorably with that of a blunt-leading-edge flat plate having the same leading-edge radius.

Circumferential afterbody surface-pressure ratios for several afterbody stations (s/R) are shown in figure 8 for angles of attack of 0° and 33° . At an angle of attack of 0° (fig. 8(a)), the pressure ratio for s/R = 1.34 (attached flow) is essentially constant with ϕ . However, the data for s/R = 1.69 indicate the possible existence of a pressure relieving effect around the model with the pressure decreasing in the direction of the model support. This effect was also observed in references 1 and 2 and was believed to be due to interference of the model support. It was noted in reference 2 that variation in the side model support configuration produced no significant differences in pressure level or variation of pressure with ϕ . Although the model support of the present





investigation was constructed to produce low interference, the effect of its presence is not completely known. Figure 8(b) shows that at an angle of attack of 33° , the afterbody pressure decreases from a maximum value on the most windward meridian ($\phi = 0^{\circ}$) to a minimum value on the meridian at which $\phi = \pm 135$, as expected.

Afterbody Flow Pattern

As discussed in the previous section, afterbody surface-pressure measurements for $0^{\rm O}$ angle of attack indicated that the flow separated between values of s/R of 1.34 and 1.69. In order to determine the point of flow separation more accurately, a tuft study was performed on the model afterbody along the meridian at which $\phi = 0^{\rm O}$. This study was conducted on a heat-transfer model (see "Model and Support System" section). The instrumentation leads which exit from the rear portion of the afterbody were assumed to have a negligible effect on the tuft results.

The motion of the tufts, as recorded on 16-mm film at 4200 frames per second, is presented in figure 9 for two tunnel tests denoted as A and B. Enlargements of the 16-mm film show that for both tunnel runs A and B, the three foremost tufts are under the influence of a high surface shear and thus are assumed to be in the attached flow region. Although the tuft adjacent to this first group indicates a slight rearward deflection, the flow was assumed to separate upstream of this tuft at a value of s/R of approximately 1.4. The four most rearward tufts experienced a forward deflection, an indication of reverse flow in the separation region. Reverse flow in the separation region was also observed in references 2 and 5, at Mach numbers 8 and 13.8, respectively.

The oil-flow technique was previously untried in the present facility and thus the results are very preliminary in nature. The enlargements for tunnel run A (fig. 9(a)) show that the vacuum-pump oil and lampblack mixture flowed rearward with time, indicating that the flow remained attached to an afterbody station of $s/R \approx 1.2$. An attempt to examine oil flow farther rearward on the model afterbody proved only partially successful (tunnel run B) and hence is not discussed.

Comparison of Afterbody Results

Figure 10 presents a comparison of the present afterbody pressure data with the data of other investigations conducted in air and nitrogen for Mach numbers 8 to 19 (refs. 2, 4, 5, 6, and 12) and in helium for Mach numbers 10 to 24.5 (refs. 6, 10, and 11). The shaded symbols in figure 10 represent free-flight measurements presented in reference 6. All the pressure distributions presented in figure 10 are along the meridian at which $\phi = 0^{\circ}$.



At 0° angle of attack (fig. 10(a)), the afterbody pressure distributions of references 2, 4, 10, and 11 are essentially invariant with variations in s/R for the instrumented range of s/R, an indication that the flow separated upstream of the pressure orifices. The present data and those of reference 5, obtained in an arc-heated facility at a nominal Mach number of 13.8 in air, demonstrate a rise in afterbody pressure ratio with an increase in the ratio s/R and thus indicate flow separation within the region of measurements. Oil-flow results of reference 5 revealed that the flow remained attached around the model corner to an afterbody station of s/R = 1.2. The findings of references 2 and 8 for Mach numbers in air of 8 and 3.29, respectively, showed that the flow

separated immediately downstream of the point where the model corner became tangent to the free-stream flow direction (s/R \approx 1.1). Thus, the results of references 2 and 5 together with the present results show that the point of laminar flow separation moves downstream on the model afterbody as the Mach number is increased from 8 to 20. The trends of the free-flight data of reference 6 are supported by the other data in figure 10(a), in that the values of the afterbody pressure ratio obtained in air or nitrogen are substantially higher than the values obtained in helium. However, for 33° angle of attack (fig. 10(b)), the pressure ratios obtained in air and nitrogen are in good agree-

ment with those obtained in helium; these results also support the trends of the free-

Figure 11 illustrates the variation of the ratio of the afterbody surface pressure in the separation region to the free-stream static pressure with the free-stream Mach number for 0° angle of attack and a range of γ_2 from approximately 1.3 to 1.67. The static-pressure ratio increases with increasing Mach number for air and nitrogen and for helium. This result is in accordance with the predictions of references 22 and 23 concerning blunt axisymmetric bodies at hypersonic Mach numbers. The afterbody pressure ratio in the separation region of the present investigation (γ_2 = 1.3) is approximately twice those of references 6, 10, and 11 in helium (γ_2 = 1.67) for a Mach number of approximately 20.

As discussed previously, the present results for $0^{\rm O}$ angle of attack show flow separation to occur at a value of s/R of approximately 1.4. However, the Mach 20 helium results of reference 10 showed that the flow separated at a value of s/R of approximately 1.1 for $0^{\rm O}$ angle of attack. The computed local Mach number for the present investigation at s/R = 1.34 and that for reference 5 at s/R = 1.2 were found to be equal to that for the helium investigation of reference 10 at the point of flow separation. However, the helium required an expansion angle only 0.69 times the expansion angle of the air and nitrogen flow to achieve this Mach number. Because of the differences in the point of flow separation and angle of flow separation with respect to the free-stream direction between the present results and the Mach 20 helium results of reference 10, helium simulation of afterbody flow expansion characteristics in air or nitrogen for



flight results of reference 6.



the Apollo configuration at $0^{\rm O}$ angle of attack is not feasible for the high hypersonic Mach number regime.

CONCLUSIONS

Measured pressure distributions on the Apollo reentry configuration along with schlieren photographs of the bow-shock-wave shapes and photographs of the afterbody tuft-flow patterns were obtained in the Langley hotshot tunnel. The investigation was performed for angles of attack of $0^{\rm O}$ and $33^{\rm O}$ at a Mach number of approximately 20 and a free-stream Reynolds number, based on maximum model diameter, of approximately $1 \times 10^{\rm 5}$ in nitrogen. Analysis of the results from the present investigation and comparison with results from other investigations has led to the following conclusions:

- 1. At an angle of attack of 0° for the present investigation, the flow remained attached around the model corner onto the afterbody and separated at a point where the ratio of the surface distance from the model axis of symmetry to the maximum model radius (s/R) was approximately 1.4. Comparison of this result with those obtained at Mach numbers 8 and 13.8 in air showed a trend of rearward movement of the point of flow separation from s/R \approx 1.1 at Mach 8 to s/R \approx 1.4 at Mach 20.
- 2. For a 33° angle of attack, comparison of the afterbody pressure distribution along the most windward meridian ($\phi = 0^{\circ}$) with that from a flat-plate investigation at a Mach number of approximately 20 showed good agreement between the afterbody pressure distribution of the Apollo model and that of a blunt-leading-edge flat plate having a leading-edge radius equal to the corner radius of the Apollo model. Blast-wave theory adequately predicted the afterbody pressure distribution along this most windward meridian.
- 3. The present afterbody surface pressure in the attached flow region for a $0^{\rm O}$ angle of attack was approximately three times the computed free-stream static pressure and approximately 30 percent greater than the prediction of Prandtl-Meyer theory for attached flow. The afterbody pressure was constant in the separation region along the meridian at which $\psi = 0^{\rm O}$ and was approximately 10 times the free-stream pressure. The tuft results indicated reverse flow in the separation region.
- 4. Discrepancy in the point of flow separation and the angle of flow separation between the present results at 0° angle of attack and those obtained at a Mach number of 20 in helium showed that helium simulation of Apollo afterbody flow expansion characteristics in air or nitrogen is not feasible for this Mach number regime.

Langley Research Center,
National Aeronautics and Space Administration,
Langley Station, Hampton, Va., March 10, 1966.





APPENDIX

CONVERSION OF U.S. CUSTOMARY UNITS TO SI UNITS

The International System of Units (SI) was adopted by the Eleventh General Conference on Weights and Measures held in Paris, October 1960 in Resolution No. 12 (ref. 24). Conversion factors required for units used herein are given in the following table:

| Physical quantity | U.S. Customary Unit | Conversion factor (*) | SI Unit |
|-------------------|------------------------|-----------------------------|--|
| Length | in. | 0.0254 | meters (m) |
| Pressure | lbf/in ² | $6.895 	imes 10^3$ | newtons/meter ² (N/m ²) |
| Temperature | $^{ m o}_{ m R}$ | 0.556 | degrees Kelvin (^o K) |

^{*}Multiply value in U.S. Customary Unit by conversion factor to obtain equivalent value in SI Unit.

Prefixes to indicate multiples of units are as follows:

| Prefix | Multiple |
|-----------|----------|
| centi (c) | 10-2 |
| mega (M) | 10^{6} |
| milli (m) | 10-3 |

12



REFERENCES

- Romeo, David J.: Experimental Results of the Pressure Distribution on a Blunt-Nose Conical-Afterbody Lunar-Mission Spacecraft with Four Nose-Edge Radii for a Mach Number of 6.0 and an Angle-of-Attack Range of 0^o to 50^o. NASA TM X-705, 1962.
- 2. Jones, Robert A.: Experimental Investigation of the Overall Pressure Distribution, Flow Field, and Afterbody Heat-Transfer Distribution of an Apollo Reentry Configuration at a Mach Number of 8. NASA TM X-813, 1963. (Supersedes NASA TM X-699.)
- 3. Gray, J. Don; and Jones, J. H.: Force and Pressure Tests on Apollo Configurations at Mach 1.5 Through 10. AEDC-TDR-63-17, U.S. Air Force, Feb. 1963.
- 4. Fox, George L.; and Marvin, Joseph G.: An Investigation of the Apollo Afterbody Pressure and Heat Transfer at High Enthalpy. NASA TM X-1197, 1966.
- 5. Lee, George; and Sundell, Robert E.: Heat-Transfer and Pressure Distributions on Apollo Models at M = 13.8 in an Arc-Heated Wind Tunnel. NASA TM X-1069, 1965.
- 6. Kemp, Joseph H., Jr.: Telemetry Measurements of the Afterbody Pressures on Free-Flying Models of the Apollo Capsule at Mach Numbers From 10 to 21 in Helium and 14 in Air. NASA TM X-1154, 1965.
- 7. Akin, Clifford M.: Experimental Comparison of Apollo Afterbody Heating in Air and CO₂. NASA TM X-1204, 1966.
- 8. Stivers, Louis S., Jr.: Effects of a Sting Support on the Supersonic Force and Moment Characteristics of an Apollo Model at Angles From -30° to +185°. NASA TM X-1081, 1965.
- 9. Marvin, Joseph G.; Tendeland, Thorval; and Kussoy, Marvin: Apollo Forebody Pressure and Heat-Transfer Distributions in Helium at M_{∞} = 20. NASA TM X-854, 1963.
- 10. Marvin, Joseph G.; and Kussoy, Marvin: Experimental Investigation of the Flow Field and Heat Transfer Over the Apollo-Capsule Afterbody at a Mach Number of 20. NASA TM X-1032, 1965.
- 11. Watson, Ralph; and Wagner, Richard D., Jr.: Pressure Distribution at a Mach Number of 24.5 on a Symmetrical Blunt-Faced Reentry Body at Angles of Attack From 0° to 40° in Helium Including an Investigation of Afterbody Sting Effects. NASA TM X-841, 1963.





- 12. Knox, E. C.: Heat-Transfer and Pressure Distributions Measured on the Apollo Command-Module Re-Entry Configuration at Mach Number 19. AEDC-TDR-63-42, U.S. Air Force, Mar. 1963.
- 13. Smith, Fred M.; Harrison, Edwin F.; and Lawing, Pierce L.: Description and Initial Calibration of the Langley Hotshot Tunnel With Some Real-Gas Charts for Nitrogen. NASA TN D-2023, 1963.
- 14. Miller, Charles G., III; Creel, Theodore R., Jr.; and Smith, Fred M.: Calibration Experience in the Langley Hotshot Tunnel for Mach Numbers From 12 to 26. NASA TN D-3278, 1966.
- 15. Smotherman, W. E.: A Miniature Wafer-Style Pressure Transducer. AEDC-TR-60-11, U.S. Air Force, Oct. 1960.
- 16. Smotherman, W. E.; and Maddox, W. V.: Variable Reluctance Pressure Transducer Development. AEDC-TDR-63-135, U.S. Air Force, July 1963.
- 17. Miller, Charles G., III: An Experimental Investigation of Support Interference on a Blunt Body of Revolution at a Mach Number of Approximately 20. NASA TN D-2742, 1965.
- 18. Grabau, Martin; Humphrey, Richard L.; and Little, Wanda J.: Determination of Test-Section, After-Shock, and Stagnation Conditions in Hotshot Tunnels Using Real Nitrogen at Temperatures From 3000 to 4000^o K. AEDC-TN-61-82, U.S. Air Force, July 1961.
- 19. Kaattari, George E.: Predicted Gas Properties in the Shock Layer Ahead of Capsule-Type Vehicles at Angles of Attack. NASA TN D-1423, 1962.
- 20. Kaattari, George E.: Shock Envelopes of Blunt Bodies at Large Angles of Attack. NASA TN D-1980, 1963.
- 21. Love, Eugene S.; Henderson, Arthur, Jr.; and Bertram, Mitchel H.: Some Aspects of Air-Helium Simulation and Hypersonic Approximations. NASA TN D-49, 1959.
- 22. Ferri, Antonio; and Pallone, Adrian: Note on the Flow Fields on the Rear Part of Blunt Bodies in Hypersonic Flow. WADC Tech. Note 56-294, U.S. Air Force, July 1956.
- 23. Whitfield, Jack D.; and Potter, J. Leith: On Base Pressures at High Reynolds Numbers and Hypersonic Mach Numbers. AEDC-TN-60-61, U.S. Air Force, Mar. 1960.
- 24. Mechtly, E. A.: The International System of Units Physical Constants and Conversion Factors. NASA SP-7012, 1964.

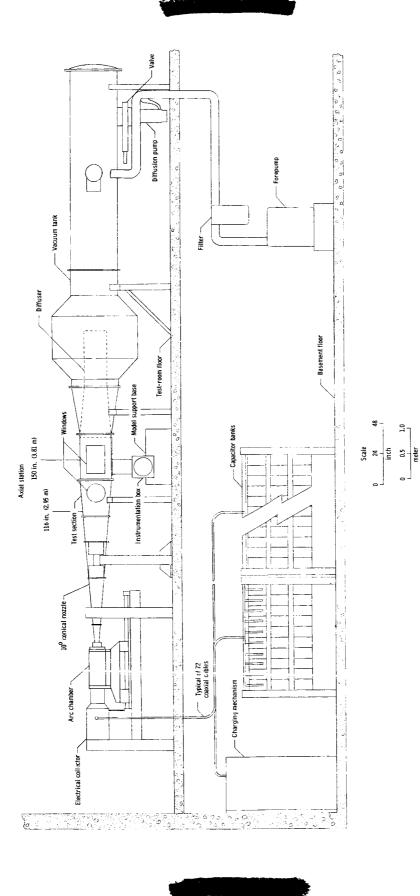
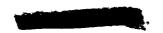


Figure 1.- Elevation view of Langley hotshot tunnel.



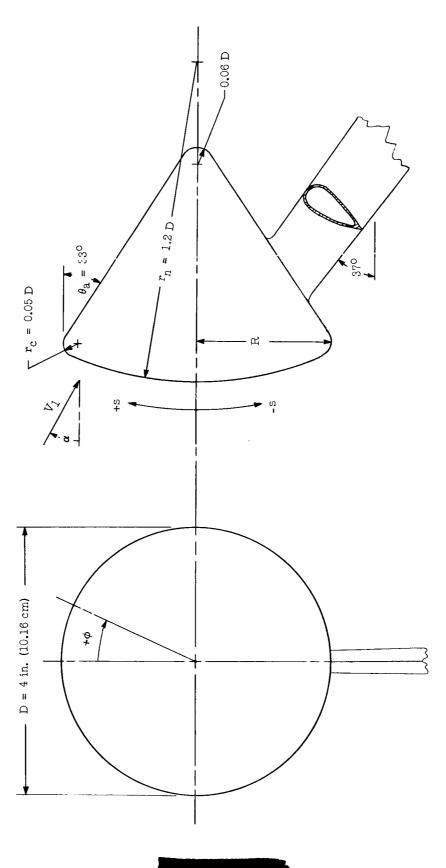
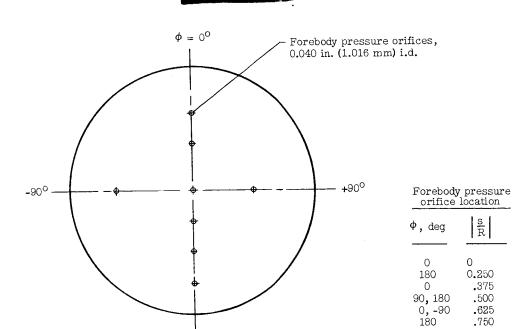


Figure 2.- Sketch of model.



Forebody (viewing downstream)

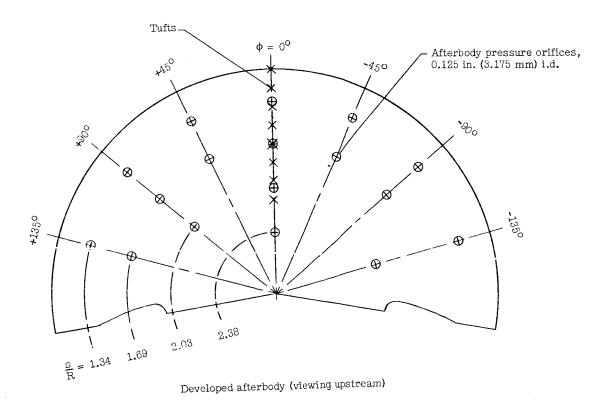
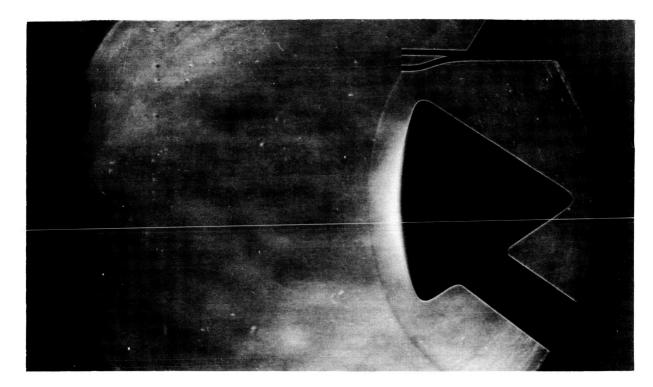


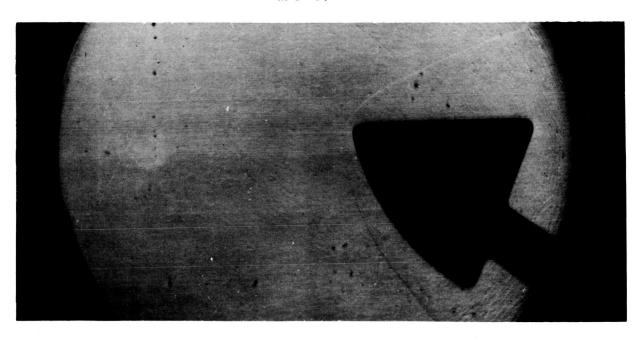
Figure 3.- Forebody and developed afterbody illustrating pressure-orifice and tuft locations.







(a) $\alpha = 0^{\circ}$.



(b) $\alpha = 33^{\circ}$.

Figure 4.- Representative schlieren photographs of bow-shock-wave shapes at $\,$ M $_{1}\approx\,$ 20.

L-66-1105





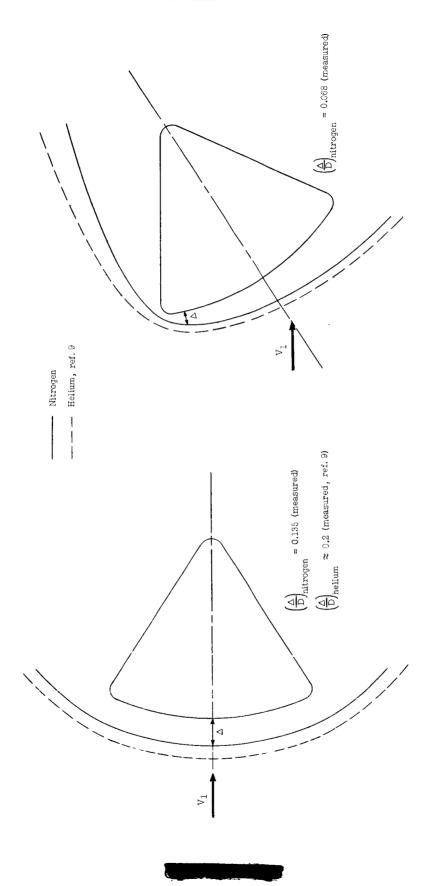


Figure 5.- Comparison of measured bow-shock-wave shapes for nitrogen and helium at $\,{\rm M}_1\approx 20.$

(a) $\alpha = 0^{0}$.

(b) $\alpha = 33^{\circ}$.



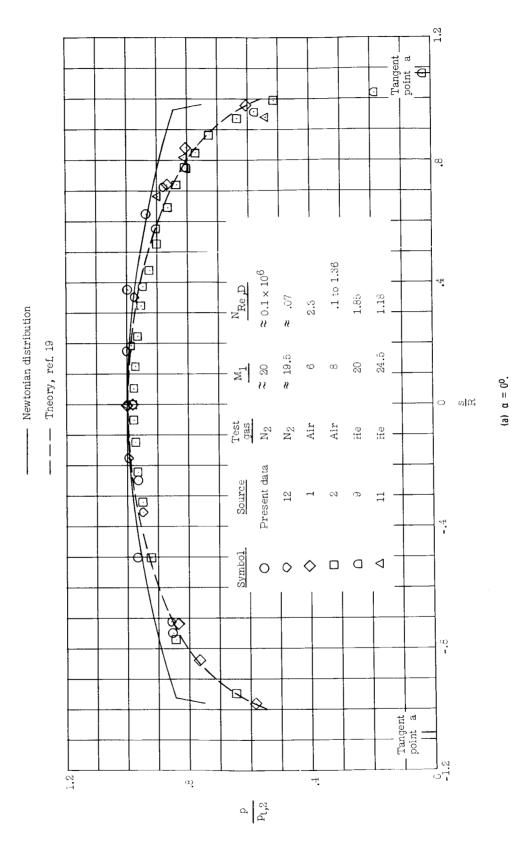
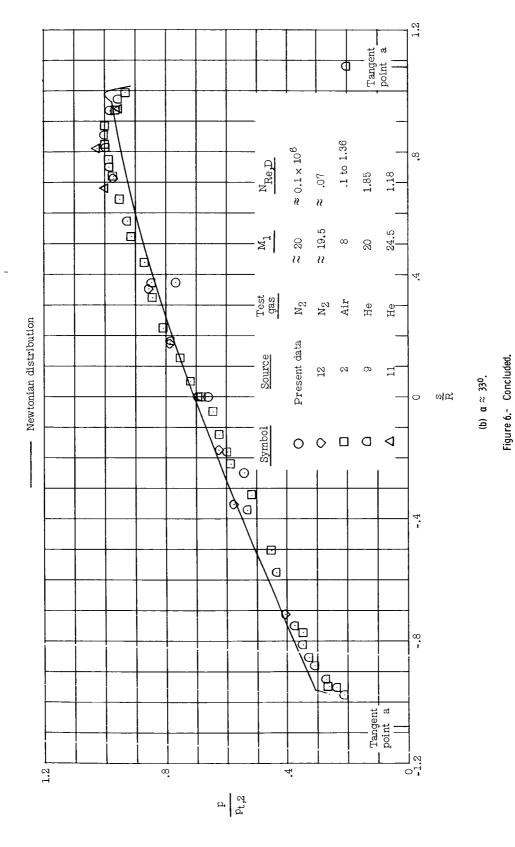
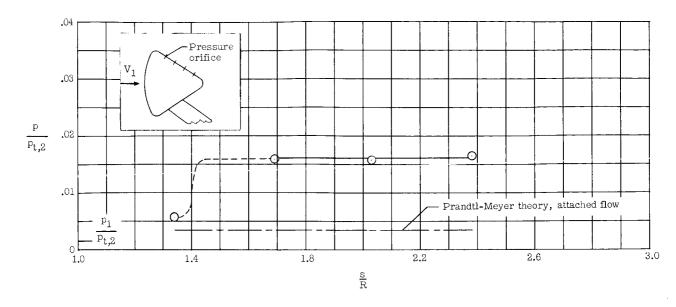


Figure 6.- Forebody pressure distribution in vertical plane of symmetry.











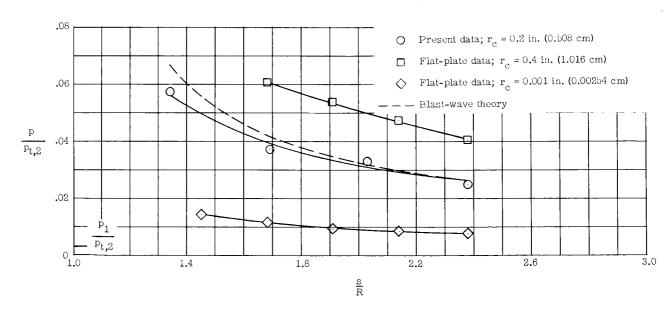
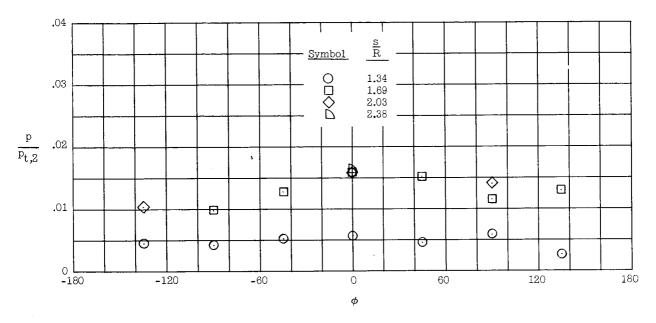


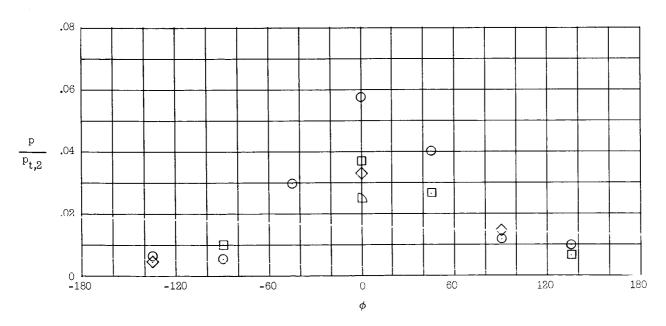
Figure 7.- Afterbody surface pressure distribution along meridian at which $\,\Phi\,$ = $\,0^{0}$. $\,M_{1}\,$ $pprox\,$ 20.

(b) $\alpha = 33^{\circ}$.





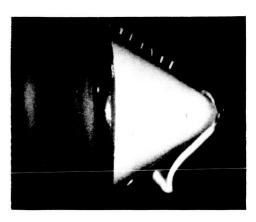




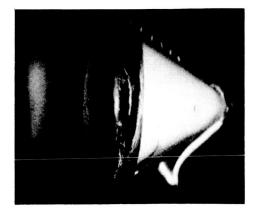
(b) $\alpha = 33^{\circ}$.

Figure 8.- Afterbody surface pressure as a function of $\,\Phi\,$ for various values of $\,$ s/R. $\,$ M $_{1} \approx \,$ 20.

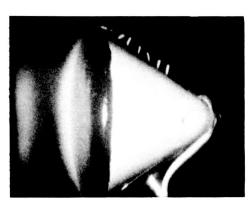




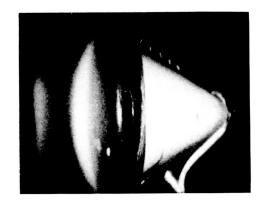
No flow



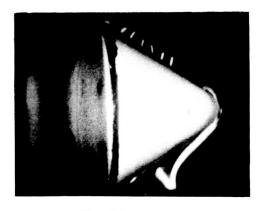
No flow



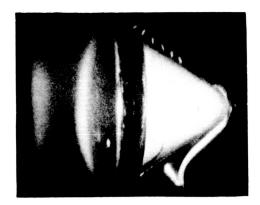
Flow, t $\stackrel{\sim}{\sim}$ 20 msec



Flow, t \approx 30 msec



Flow, t \approx 90 msec



Flow, t \approx 80 msec

(a) Tunnel run A.

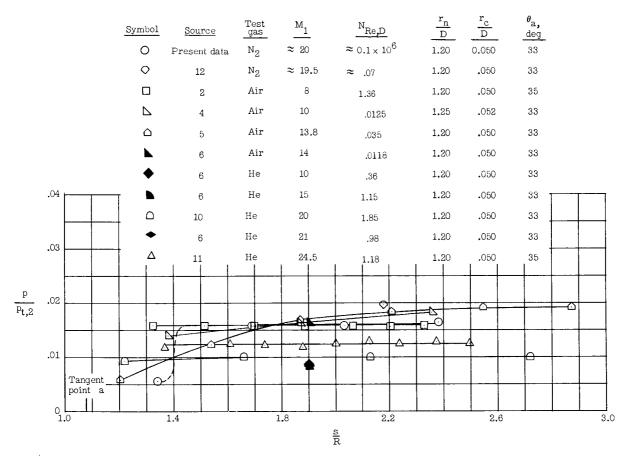
(b) Tunnel run B.

L-66-1106

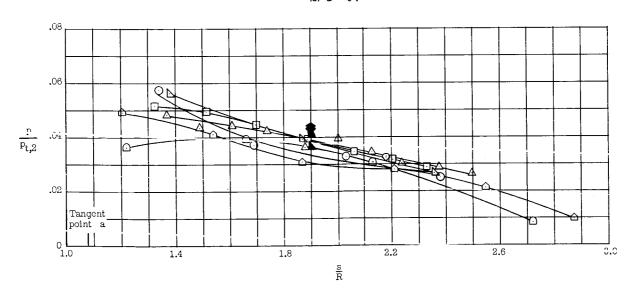
Figure 9.- Tuft and oil-flow study at 0° angle of attack. $\,\text{M}_{1}\,\approx\,$ 20.











(b) $\alpha \approx 33^{\circ}$.

Figure 10.- Comparison of afterbody pressure distributions along meridian at which $\Phi = 0^{\circ}$. (Shaded symbols denote free-flight data, ref. 6.)





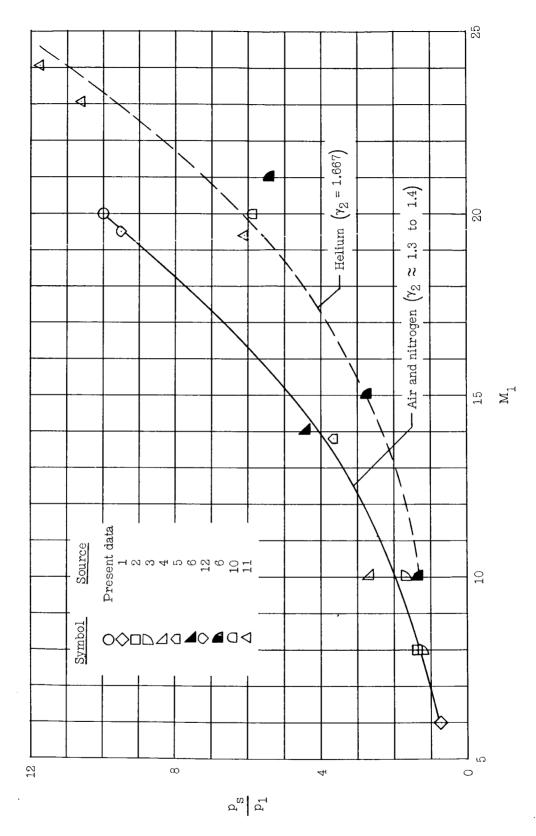


Figure 11.- Variation of afterbody pressure in separation region with free-stream Mach number. $\alpha = 0^{\circ}$. (Shaded symbols denote free-flight data, ref. 6.)